Original Article

Latin American Journal of Solids and Structures

www.lajss.org

Numerical analysis of RC plane structures: a concentrated nonlinear effect approach

Abstract

The present work aims to study the nonlinear behavior of reinforced concrete structures via Refined Plastic Hinge Method (RPHM). Pseudo-springs are used at the finite element ends, where the gradual loss of stiffness is determined by the combination of the normal force and bending moment (NM) in the cross section. The limiting of the uncracked, elastic and plastic regimes is done in the NM diagram. The concrete cracking is explicitly simulated with two approaches to calculate the effective moment of inertia of the cross section. The displacement-based formulation is referenced to the co-rotational system and coupled with continuation strategies to allow to overcome the possible critical points in the equilibrium paths. For validation of the numerical simulations, the results found with the proposed formulation are confronted with experimental and numerical data present in literature.

Keywords

RC Structures, interaction curves, cracking, concentrated plasticity

Í. J. M. Lemes [a*]
R. C. Barros [b]
R. A. M. Silveira [b]
A. R. D. Silva [b]
P. A. S. Rocha [b]

[a] Departamento de Engenharia, Universidade Federal de Lavras, Lavras, MG, Brasil. E-mail: igor.lemes@deg.ufla.br

[b] Departamento de Engenharia Civil, Universidade Federal de Ouro Preto, Ouro Preto, MG, Brasil. E-mail: rafaelcesario@hotmail.com, ricardo@em.ufop.br, andreadias-silva@yahoo.com.br, pandrocha@gmail.com

*Corresponding author

http://dx.doi.org/10.1590/1679-78254681

Received: November 11, 2017
In Revised Form: January 25, 2018
Accepted: February 09, 2018
Available online: March 20, 2018

1 INTRODUCTION

The use of high strength materials results in increasingly slender sections and under these conditions, there are large displacements and strains, which give rise to the so-called nonlinear effects. The concrete constitutive relationship is naturally nonlinear and not even isotropic, since the concrete tensile strength is much lower than that of compression (about 1/10 of the compressive strength; Carvalho and Figueiredo Filho, 2014). On the other hand, the steel behavior can be considered isotropic when the stress-strain relationship becomes nonlinear after reaching the yield.

Due to these sources of nonlinearity, numerical models are developed aiming at a more realistic study of these structural systems behavior. This procedure is encouraged by current design codes (Stramandinoli, 2007). Bratina et al. (2004) emphasize that the evolution of the numerical methodologies for RC structure analysis has positively influenced the prediction of the structural behavior.

The search for numerical formulation generalization and efficiency has prompted the use of distributed plasticity-based methods, commonly referred to as the Plastic Zone Method (PZM) (Spacone et al., 1996; Bratina et al., 2004; Sousa Jr and Caldas, 2005; Sousa Jr and Muniz, 2007; Kostic and Filippou, 2012; Parente Jr et al., 2014). In this approach, formulation considers the strains directly, allowing the modeling of anisotropic behavior of concrete elements. Although it is considered to be more accurate, PZM requires intense computational effort (Chen and Kim, 1997). As an alternative solution, Scott and Fenves (2006), Ngo-Huu and Kim (2012) and others treated the finite element central region as linear-elastic, and in pre-defined lengths near the nodal points the inelastic behavior was evaluated.

In contrast, there is the Refined Plastic Hinge Method (RPHM), which considers plasticity only at the nodal points of the element. Even though it is simpler, recent research has demonstrated that RPHM presents considerable accuracy in numerical responses (Liu et al. 2012b; Fong and Chan, 2012; Lemes et al., 2016, Lemes et al., 2017a, Lemes et al., 2017b, Lemes et al., 2017c). The classical RPHM approach starts from a hybrid finite element with pseudo springs at the element ends whereby the stiffness degradation of these springs is responsible for the simulation of the physical nonlinearity under the possibility of three regimes: linear-elastic, elastoplastic and plastic. The linear-elastic regime contradicts the inherently nonlinear behavior of the concrete under compression, besides there are no considerations about the cracking in this methodology (Lemes et al., 2017b). In order to correct such problems, Lemes et al. (2017c) proposed the SCM/RPHM coupling, where both the bearing capacity and the stiffness were accurately evaluated, improving the accuracy of the concentrated plasticity-based analysis.

However, appearing as an option to solve the problem in classical RPHM, is the introduction of an interaction curve to limit the uncracked state and the determination of new equations for the stiffness degradation of these reinforced concrete structures (Lemes et al., 2016). In this sense, Liu et al. (2012b) and Iu (2016) sought the feasibility analysis of these structures based on the proposal of Branson and Metz (1963), and the stiffness degradation was evaluated by the effective moment of inertia equation.

In addition to the Branson and Metz (1963) research, several works (Al-ZaidD et al., 1991; Gilbert, 1999; Tikka and Mirza, 2005; Bischoff, 2005) studied the concrete cracking effect on the behavior of RC elements by proposing explicit equations or modifications in existing equations for such an evaluation. More recently, Patel et al. (2015) presented an alternative neural network-based approach for estimating the effective moment of inertia by means of an explicit equation. From the results provided by Patel et al. (2015), it is possible to verify that there is a better adjustment of the RC beams behavior to the more precise FEM-based methodologies, if compared to the Branson and Metz (1963) proposal.

This work presents a RPHM-based approach, where the plasticity effects are treated in a concentrated way at nodal points. The cracking is treated together by explicit considerations of the cross section moment of inertia reduction due to the tensile stresses. In this sense, two proposals are tested and confronted for the nonlinear analysis of two-dimensional reinforced concrete structures. The cross section analysis as well as the definition of the elastic, inelastic, uncracked, cracked and bearing capacity regimes is done via the Strain Compatibility Method (SCM). In addition, it is proposed an adjustment for the concrete modulus of elasticity in elastic regime for the adequacy of the material constitutive relationship to the presented numerical model.

2 FINITE ELEMENT FORMULATION

2.1 Force-displacement relationship

In the present work, a RPHM-based formulation to simulate the concentrated plasticity in the nodal points is applied. In this case, the flexural stiffness degradation occurs exclusively at the nodal points. Then, the method is presented introducing the effect of geometric and material nonlinearities.

It is important to highlight some considerations involving the finite element formulation used here:

- All elements are initially straight, prismatic and the cross-section remains plane after deformation;
- The effects of global instability that may occur in three-dimensional problems (e.g., lateral and torsional buckling) are ignored considering a locking system out of plane;
- Large displacements and rigid body rotations are allowed; and
- The shear strain effects are ignored.

In the structural system modeling, the hybrid beam-column finite element of length *L*, delimited by nodal points *i* and *j* (Figure 1), is used. This element has zero-length pseudo rotational springs ($L_{ps} \rightarrow 0$) at its ends, which are responsible for the plasticity simulation by means of the parameter S_p, discussed in Section 2.2. The finite element is referenced to the co-rotational system where the degrees of freedom are the rotations at nodes *i* and *j*, given by θ_i and θ_j, and the axial displacement in *j*, δ. The terms M_i, M_j and *P* represent the bending moments and the axial force in the respective degrees of freedom.

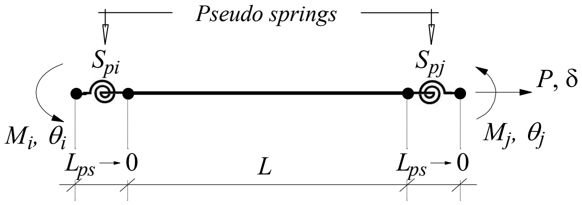

Figure 1: Hybrid finite element referenced to co-rotational system

According to Chan and Chui (2000), the pseudo-spring's relative rotation, ϕ_p, is defined between the rotation angles of the side connected to the global node of the element, θ_p, and that is connected to another beam-column element. Based on the finite element deformed configuration, by means of the bending moment action shown in Figure 2, the kinematic, constitutive and equilibrium relationships, respectively, are written as:

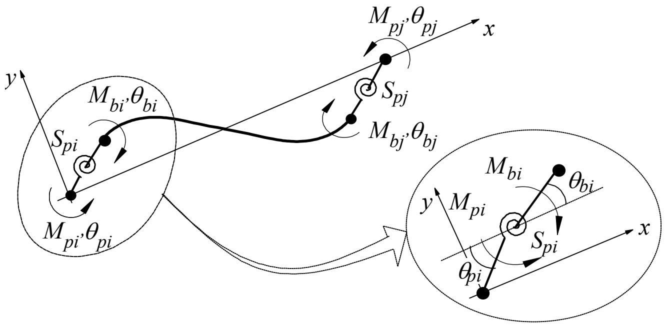

Figure 2: Deformed hybrid finite element

$$\begin{aligned} \Delta\phi_{pi} &= \Delta\theta_{pi} - \Delta\theta_{bi} \\ \Delta\phi_{pj} &= \Delta\theta_{pj} - \Delta\theta_{bj} \end{aligned} \tag{1}$$

$$\begin{aligned} \Delta M_{pi} &= S_{pi}\Delta\phi_{pi} \\ \Delta M_{pj} &= S_{pj}\Delta\phi_{pj} \end{aligned} \tag{2}$$

$$\begin{aligned} \Delta M_{pi} + \Delta M_{bi} &= 0 \\ \Delta M_{pj} + \Delta M_{bj} &= 0 \end{aligned} \tag{3}$$

in which $\Delta\phi_{pi}$ and $\Delta\phi_{pj}$ describe the incremental relative rotation's reference to material nonlinearity simulated by the pseudo-springs, ΔM_{pi} and ΔM_{pj} are the bending moments acting on the spring element ends *i* and *j*, respectively, and ΔM_{bi} and ΔM_{bj} are the bending moments at the beam member end.

The proper algebraic manipulation of Eqs. (1), (2) and (3) generate three systems of equations that represent the equilibrium of the springs in nodes *i* and *j*, as well as the equilibrium in the beam element. These systems are written in matrix form as follows:

$$\begin{Bmatrix} \Delta M_{pi} \\ \Delta M_{bi} \end{Bmatrix} = \begin{bmatrix} S_{pi} & -S_{pi} \\ -S_{pi} & S_{pi} \end{bmatrix} \begin{Bmatrix} \Delta\theta_{pi} \\ \Delta\theta_{bi} \end{Bmatrix} \tag{4}$$

$$\begin{Bmatrix} \Delta M_{pj} \\ \Delta M_{bj} \end{Bmatrix} = \begin{bmatrix} S_{pj} & -S_{pj} \\ -S_{pj} & S_{pj} \end{bmatrix} \begin{Bmatrix} \Delta\theta_{pj} \\ \Delta\theta_{bj} \end{Bmatrix} \tag{5}$$

$$\begin{Bmatrix} \Delta M_{bi} \\ \Delta M_{bj} \end{Bmatrix} = \begin{bmatrix} k_{22} & k_{23} \\ k_{32} & k_{33} \end{bmatrix} \begin{Bmatrix} \Delta\theta_{bi} \\ \Delta\theta_{bj} \end{Bmatrix} \tag{6}$$

Finally, the condensation of these three matrix relationships into a single force-displacement relationship for the hybrid finite element, considering all degrees of freedom, is defined by:

$$\begin{Bmatrix} \Delta P \\ \Delta M_{pi} \\ \Delta M_{pj} \end{Bmatrix} = \begin{bmatrix} k_{11} & 0 & 0 \\ 0 & S_{pi} - \dfrac{S_{pi}^2\left(S_{pj} + k_{33}\right)}{\beta} & \dfrac{S_{pi}k_{23}S_{pj}}{\beta} \\ 0 & \dfrac{S_{pj}k_{32}S_{pi}}{\beta} & S_{pj} - \dfrac{S_{pj}^2\left(S_{pi} + k_{22}\right)}{\beta} \end{bmatrix} \begin{Bmatrix} \Delta\delta \\ \Delta\theta_{pi} \\ \Delta\theta_{pj} \end{Bmatrix} \tag{7}$$

in which $\beta = \left(S_{pi} + k_{22}\right)\left(S_{pj} + k_{33}\right) - k_{32}k_{23}$.

The terms k_{11}, k_{22}, k_{23}, k_{32}, and k_{33} are components of the beam-column stiffness matrix element, without the pseudo-springs, described by Lemes et al. (2017c) as:

$$k_{11} = \frac{E_c A}{L} \tag{8}$$

$$k_{22} = \frac{E_c\left(3I_{eq,i} + I_{eq,j}\right)}{L} + \frac{2PL}{15} \tag{9}$$

$$k_{23} = k_{32} = \frac{E_c\left(I_{eq,i} + I_{eq,j}\right)}{L} - \frac{PL}{30} \tag{10}$$

$$k_{33} = \frac{E_c\left(I_{eq,i} + 3I_{eq,j}\right)}{L} + \frac{2PL}{15} \tag{11}$$

where P is the internal axial force, A is the cross-section area, I_{eq} is the effective moment of inertia according to Branson and Metz (1963) (BM equation) or Patel et al. (2015) (P equation) proposals, evaluated at nodal points i and j, and L is the finite element length.

The elasticity modulus of concrete, E_c, is obtained in a particular way. Liu et al. (2012b) and Iu (2016) used the initial tangent modulus of elasticity (E_{ci}) as E_c, illustrated in Figure 3. This ends up overestimating the value of the modulus of elasticity, since by the nonlinear concrete behavior under compression, low strain rates imply a reduction of the modulus of elasticity. On the other hand, the use of the elastic secant modulus, E_{csi}, between 0 and (ε_{cin}, f_{cin}) (Izzuddin and Smith, 2000) points, generates conservative results for low strain values. Thus, it is proposed to use the mean value between E_{ci} and E_{csi} for E_c, that is used in global structural analysis. The values of ε_{cin} and f_{cin} can be easily calculated considering the Hooke's equation ($f_c = E_{ci}\,\varepsilon$) and NBR-6118 (2014) constitutive relationship, resulting in $\varepsilon_{cin} = \varepsilon_{ci}/2$ and $f_{cin} = 0.75 f_c$. Thus, $E_{csi} = 1.75\, f_c/\varepsilon_{cin}$.

It should be noted in Eqs. (8)-(11) that there is an additional terms related to bending. This part refers to the consideration of geometric nonlinearity, which is introduced in this methodology through a simplified formulation proposed by Yang and Kuo (1994). The option to define simplified terms was made by previous numerical studies, where high order terms had little influence on the global response of the small-sized RC systems simulated (Lemes et al., 2017c).

The co-rotational system transformation to local and global systems as well as the return mapping strategy adopted here can be seen in Lemes (2015).

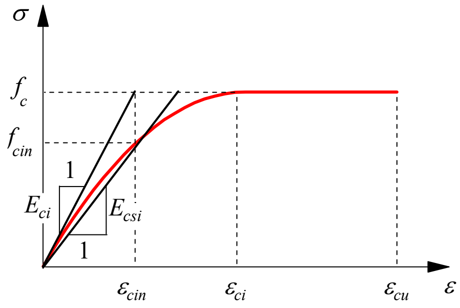

Figure 3: *Concrete stress-strain relationship under compression: elastic limit strain and modulus of elasticity*

2.2 Pseudo-springs rotational stiffness

As already mentioned, in the RPHM the cross-section flexural stiffness degradation, simulating plasticity is done by pseudo-springs. Thus, it is necessary to obtain stiffness degradation forms for these springs that are consistent with the material employed in the cross-section. The original RPHM proposal was developed for steel elements with perfect elastoplastic behavior. When it comes to RC elements the original methodology must be modified as proposed in the present work.

Figure 4 illustrates three interaction curves for a specific cross-section: the full yield curve – indicates the bearing capacity; the initial yield curve – defines the elastic region; and the initial cracking curve – delimits the uncracked state of the cross-section. These curves are the result of a combination of axial force and a bending moment acting around one of the main axes bending.

Obviously, an initial cracking curve was not necessary in the original RPHM proposal (Chan and Chui, 2000), since it was exclusively applied for structural steel systems. However, in the evolution of the method, it is noticed the necessity to introduce this curve to better approximate the actual RC structural behavior as observed by Lemes et al. (2017b).

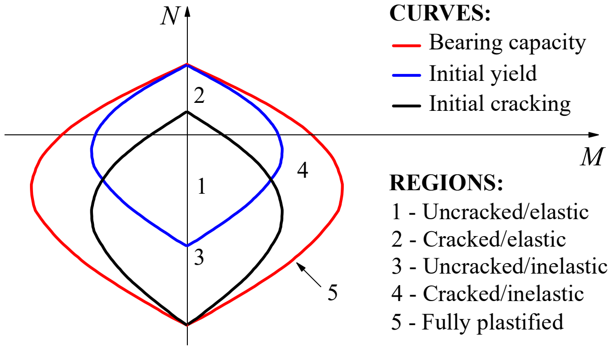

Figure 4: Interaction NM Curves and spring rotational stiffness degradation regions

In Figure 4, it is also possible to observe four regions. Thus, expression definitions for the simulation of pseudo-spring stiffness in each of the described regions are required.

According to the classical RPHM, three equations define the pseudo-spring stiffness for the previously mentioned regions. In regions 1 and 2, it is observed that the section is in an elastic regime. In regions 3 and 4, there can be noticed that the section is in a stiffness degradation process due to plastic strains. And finally, for when the fully plastified section occurs (region 5). For a given axial force-bending moment combination, S_p is defined as follow:

$$If \quad M \leq M_{er} : \quad S_p = 1 \times 10^{10} \tag{12}$$

$$If \quad M_{er} < M < M_{pr} : \quad S_p = \frac{E_c I_{eq}}{L} \left(\frac{M_{pr} - M}{M - M_{er}} \right) \tag{13}$$

$$If \quad M = M_{pr} : \quad S_p = 1 \times 10^{-10} \tag{14}$$

in which L is the finite element length, M_{pr} and M_{er} are the full and initial yield bending moment reduced by the combined action to an axial force, and $E_c I_{eq}$ is the section's flexural stiffness, considering the cracking, as discussed in the next Section 2.3.

Note that, by the value described in Eq. (12), there is no possibility of simulating cracking in the elastic regime. This adjustment is made in the following section.

2.3 Concrete cracking approach

As previously pointed out, there is no specific equation for simulating the cracking using the pseudo-spring's rotational stiffness, S_p. Thus, it is intended to use Eq. (12). When the pseudo-spring's stiffness is infinite, or numerically treated as such, the limit for $S_p \rightarrow \infty$ causes the terms k_{22}, k_{23}, k_{32} and k_{33} to converge to the values assigned in Eqs. (9), (10) and (11). Then, for the terms expressed in the equations, the moment of inertia can be modified following two proposals.

Branson and Metz (1963) proposed a simple equation (BM equation) for the effective moment of inertia evaluation of RC sections in a cracking state. This equation is used by some design codes, such as NBR-6118 (2014), ACI-318 (2008), among others. The moment of inertia is given by (Branson and Metz, 1963):

$$If \quad M > M_{cr} : \quad I_{eq} = \left(\frac{M_{cr}}{M} \right)^3 I_c + \left[1 - \left(\frac{M_{cr}}{M} \right)^3 \right] I_{cr}, \quad I_{eq} \leq I_c \tag{15}$$

$$If \quad M \leq M_{cr} : \quad I_{eq} = I_c \tag{16}$$

where M_{cr} and M are, respectively, the initial cracking bending moment and the bending moment acting on the section, I_c is the intact section moment of inertia (initial slope of the bending moment–curvature for zero axial force with no tensile stress in concrete), and I_{cr} is the cracked moment of inertia of the section evaluated in the critical point of moment-curvature relationship (Section 3).

Patel et al. (2015) presented an alternative neural network-based approach for estimating effective moment of inertia by means of an explicit equation (P equation), which is described as:

$$I_{eq} = \frac{3I_c}{1 + e^{-\left[7.4688 + \sum_{k=1}^{6}\left(\frac{a_k}{1+e^{H_k}}\right)\right]}} \tag{17}$$

$$H_k = b_k\,\rho_t + c_k\frac{I_{cr}}{I_c} + d_k\frac{M_{cr}}{M} + e_k \tag{18}$$

where a_k, b_k, c_k, d_k and e_k are described in Table 1.

2.4 Nonlinear structural static problem solution

In FEM context, the nonlinear static solver consists of obtaining the equilibrium between internal and external forces for each load increment as follows:

$$\mathbf{F}_{e,g} - \mathbf{F}_{i,g} \cong \mathbf{0} \rightarrow \lambda\mathbf{F}_r - \mathbf{F}_{i,g} \cong \mathbf{0} \tag{19}$$

Table 1: P equation parameters (Patel et al., 2015).

Parameter	k					
	1	2	3	4	5	6
a	8.7116	-0.3754	11.6985	-10.7167	0.6177	22.9397
b	-0.1978	4.3806	2.8322	3.0191	10.1889	-3.7310
c	1.2333	-22.0048	-4.1654	-4.3927	-15.7592	5.4520
d	0.0011	-0.1823	9.4775	9.7598	5.0682	-0.0189
e	-0.0386	6.2396	-6.7756	-7.1914	-3.2443	-2.9660

where $\mathbf{F}_{i,g}$ and $\mathbf{F}_{e,g}$, are the global internal and external force vectors, respectively, λ is the load factor and $\mathbf{F}_r$ is the reference load vector.

To solve the global nonlinear static problem, load increment and iteration strategies are used.

The initial increase of the load parameter, $\Delta\lambda^0$, is automatically determined by the technique of generalized displacement (Yang and Kuo, 1994). Thus, $\Delta\lambda^0$ is calculated as:

$$\Delta\lambda^0 = \pm\Delta\lambda_1^0\sqrt{\left|\frac{\left({}^1\delta\mathbf{U}_r^T\right)\left({}^1\delta\mathbf{U}_r\right)}{\left({}^t\delta\mathbf{U}_r^T\right)\left({}^t\delta\mathbf{U}_r\right)}\right|} = \pm\Delta\lambda_1^0\sqrt{\left|GSP\right|} \tag{20}$$

where index 1 indicates the $\Delta\lambda^0$ and $\delta\mathbf{U}_r$ (tangential nodal displacements) values obtained in the first loading step, and GSP represents the Generalized Stiffness Parameter.

In the traditional scheme of the Newton-Raphson method, the parameter load λ is kept constant throughout the iterative process. Thus, the equilibrium path can be obtained until a limit point and/or a bifurcation point is reached. The variation of λ during the iterative cycle enables the full equilibrium path to be traced. In this work, the minimum residual displacement norm strategy proposed by Chan (1988) was used. In this strategy, the correction of the load parameter $\delta\lambda^k$ is given by the equation:

$$\delta\lambda^k = -\frac{\left(\delta\mathbf{U}_r^k\right)^T\delta\mathbf{U}_g^k}{\left(\delta\mathbf{U}_r^k\right)^T\delta\mathbf{U}_r^k} \tag{21}$$

with $\delta\mathbf{U}^k_g$ being the correction obtained from the application of the Newton-Raphson method with the conventional strategy of λ increment, and $\delta\mathbf{U}^k_r$ the iterative vector displacements resulting from the application of $\mathbf{F}_r$.

Table 2 sequentially describes the solver used here for the nonlinear static problem.

3 CROSS-SECTION ANALYSIS

3.1 Materials behavior

To make an accurate analysis of cross-sectional nonlinear behavior under external loads, a correct description of the materials behavior is required.

The concrete has different mechanical properties for tensile strength and compression. When tensioned, this material has a tensile strength f_{cr}. It is also noteworthy that upon reaching f_{cr} stress, the cracking process begins. For strains exceeding ε_{cr}, the concrete loses strength. Thus, many researchers and even the design codes disregard their contribution when tensioned (Sousa Jr. and Caldas, 2005; Fong and Chan, 2012). In this study, the constitutive relationship proposed by NBR-6118 (2014) is used to describe the behavior of concrete under compression; for tension, this study used the model proposed by Vecchio and Collins (1986). That is:

Table 2: Numerical strategy for solving the nonlinear structural problem.

```
Algotithm: Nonlinear structural static analysis
1.  Read the input data: geometric, material and loading properties of the structural system
2.  Form the interaction curves (initial cracking, initial yield, bearing capacity)
3.  Obtain the reference nodal load vector, $\mathbf{F}_r$ (loading direction)
4.  $t = 0$
5.  $t_1 = t$
6.  Initial conditions: ${}^t\mathbf{U} = \mathbf{0}$ and ${}^t\lambda = 0$
7.  for each load increment do → INCREMENTAL LOAD PROCESS
8.      $t = t_1$ → Previous load step
9.      $t_1 = t + 1$ → Current load step
10      Form the structural system tangent stiffness matrix: $\mathbf{K}$
11.     Solve for the tangent displacement vector: $\delta\mathbf{U}_r = \mathbf{K}^{-1}\mathbf{F}_r$
12.     if $t_1 = 1$ then
13.         $\Delta\lambda^0 = (\Delta\lambda^0)_1$
14.     else
15.         Define: $\Delta\lambda^0$ (Eq. 20)
16.     end if
17.     Evaluate the initial incremental displacement vector: $\Delta\mathbf{U}^0 = \Delta\lambda^0\, \delta\mathbf{U}_r$
18.     Update variables in $t_1$: ${}^{t_1}\lambda = {}^t\lambda + \Delta\lambda^0$ and ${}^{t_1}\mathbf{U} = {}^t\mathbf{U} + \Delta\mathbf{U}^0$
19.     for $k = 1$, $nmax$ do → ITERATIVE PROCESS
20.         Evaluate the internal forces vector: ${}^{t_1}\mathbf{F}_i^{(k-1)} = {}^t\mathbf{F}_i + \mathbf{K}\Delta\mathbf{U}^{(k-1)}$
21.         Evaluate the residual force vector: $\mathbf{g}^{(k-1)} = {}^{t_1}\lambda^{(k-1)}\, \mathbf{F}_r - {}^{t_1}\mathbf{F}_i^{(k-1)}$
22.         if $\|\mathbf{g}^{(k-1)}\| / \|\Delta\lambda^{(k-1)}\mathbf{F}_r\| \leq$ tolerance factor then
23.             Exit the iterative process and go to line 33
24.         end if
25.         if standard Newton-Raphson method then
26.             Update the tangent stiffness matrix $\mathbf{K}$
27.         end if
28.         Update the load parameter correction, $\delta\lambda^k$ (Eq. 21)
29.         Evaluate the nodal displacement correction vector: $\delta\mathbf{U}^k = \delta\mathbf{U}^k_g + \delta\lambda^k\, \delta\mathbf{U}^k_r$
30.         Update the load parameter and the nodal displacement vector:
                $\Delta\lambda^k = \Delta\lambda^{(k-1)} + \delta\lambda^k$ and $\Delta\mathbf{U}^k = \Delta\mathbf{U}^{(k-1)} + \delta\mathbf{U}^k_g + \delta\lambda^k\, \delta\mathbf{U}^k_r$
                ${}^{t_1}\lambda^k = {}^t\lambda + \Delta\lambda^k$ and ${}^{t_1}\mathbf{U}^k = {}^t\mathbf{U} + \Delta\mathbf{U}^k$
31.     end for
32.     Update the structural system variables (nodal coordinates, internal forces vector and $S_p$)
33. end for
```

$$\sigma = \begin{cases} \dfrac{f_{cr}}{1+\sqrt{500\varepsilon}}, & \varepsilon_{cr} < \varepsilon \\ E_{tr}\varepsilon, & 0 < \varepsilon \leq \varepsilon_{cr} \\ -f_c\left[\dfrac{2\varepsilon}{\varepsilon_{ci}} - \left(\dfrac{\varepsilon}{\varepsilon_{ci}}\right)^2\right], & \varepsilon_{ci} < \varepsilon \leq 0 \\ -f_c, & \varepsilon_{ci} \leq \varepsilon \leq \varepsilon_{cu} \end{cases} \tag{22}$$

where ε_{ci}, ε_{cu} and ε_{cr} are the strain limits of the nonlinear concrete behavior, the ultimate strain of the concrete in compression, and the concrete cracking strain, respectively; f_{cr} is the tensile strength and E_{tr} is the elastic tensile modulus of the concrete before cracking.

A constitutive relationship that neglects the strain hardening effects and considers a gradual transition between the elastic and plastic regimes was used to describe the steel reinforcements behavior (Caldas, 2004; Lemes, 2015). Thus:

$$\sigma = \begin{cases} E_s \varepsilon, & \left|\varepsilon\right| < \varepsilon_1 \\ \operatorname{sgn}(\varepsilon) f_y \left(c + \sqrt{c^2 + 45\left|\varepsilon\right| - 0.49} \right), & \varepsilon_1 < \left|\varepsilon\right| < \varepsilon_y \\ \operatorname{sgn}(\varepsilon) f_y, & \varepsilon_y \le \left|\varepsilon\right| \le \varepsilon_u \end{cases} \tag{23}$$

where:

$$c = 0.7 - 22.5 \frac{f_y}{E_s} \tag{24a}$$

$$\varepsilon_1 = 0.7 \frac{f_y}{E_s} \tag{24b}$$

$$\varepsilon_y = 0.002 + \frac{f_y}{E_s} \tag{24c}$$

with f_y and ε_y being respectively the steel yield stress and strain, E_s is the modulus of elasticity, and the elastic regime is limited by the strain ε_1. The steel's ultimate strain is named ε_u.

Figure 5 illustrates the uniaxial behavior of the reinforced concrete section's constituent materials.

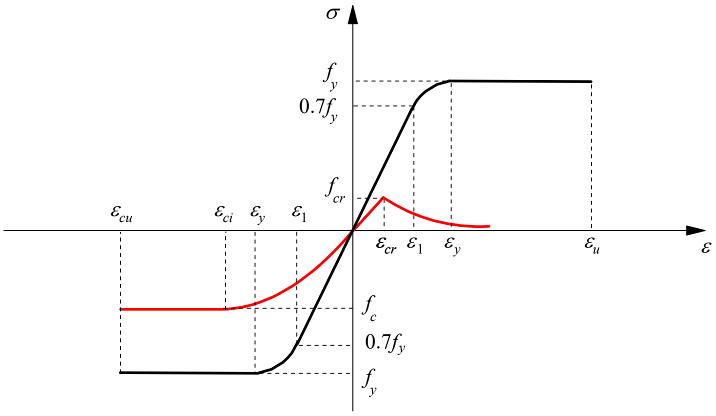

Figure 5: Constitutive relationships adopted for concrete and steel

3.2 Moment-curvature relationship

To describe the strain distribution, the cross-section discretization in layers, shown in Figure 6, is very efficient. It is done to capture the axial strain, ε in the plastic centroid (PC) of each layer, and then (through the material constitutive relationships) to obtain the respective stresses, σ_i. In this same figure, the distribution of strains in a reinforced concrete section is illustrated for a combination of axial force and bending moment. Thus, the axial strain in the ith layer is given by:

$$\varepsilon_i = \varepsilon_0 + \phi y_i \tag{25}$$

where y_i is the distance between the plastic centroids of the analyzed layer and the cross section, ε_0 is the axial strain of the PC section, and ϕ its curvature.

In the matrix notation that follows, ε_0 and ϕ are the terms of the strain vector $\mathbf{X} = [\varepsilon_0 \ \phi]^T$. Furthermore, the cross-section underformed configuration avoids convergence problems related to the balance between the external and internal forces. Numerically, it can be said that the section equilibrium is obtained when the following equation is satisfied:

$$\mathbf{F}\left(\mathbf{X}\right) = \mathbf{f}_{ext} - \mathbf{f}_{int} \cong \mathbf{0} \tag{26}$$

where the external forces vector $\mathbf{f}_{ext}$ is given by the axial force, N, and bending moment, M. In matrix form, the above equation is described as:

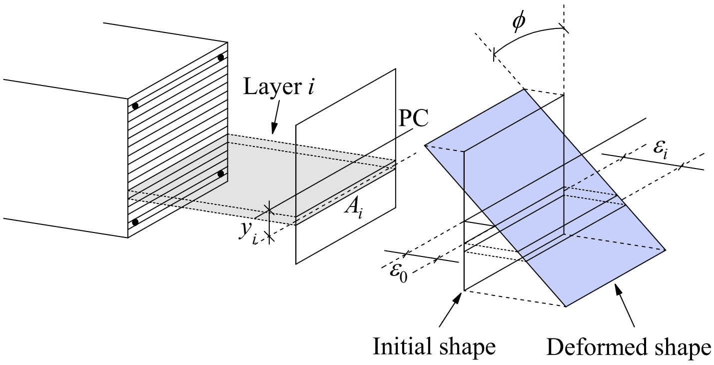

Figure 6: Linear strain field

$$\mathbf{F}\left(\mathbf{X}\right) = \begin{bmatrix} N \\ M \end{bmatrix} - \begin{bmatrix} \sum_{i=1}^{n_{lay}} \sigma\left[\varepsilon_i\left(\varepsilon_0, \phi\right)\right] A_i \\ \sum_{i=1}^{n_{lay}} \sigma\left[\varepsilon_i\left(\varepsilon_0, \phi\right)\right] y_i A_i \end{bmatrix} \tag{27}$$

in which, n_{lay} is the number of layers generated by section discretization.

The internal forces are obtained from the cross section's deformed shape through classical integrals. Once the areas A_i, and positions, y_i, of each layer are known, the integral is determined as described by the sums in Eq. (27).

Although it is efficient to start the process with $\mathbf{X} = \mathbf{0}$, convergence is achieved only in the first iteration if external forces are null. Thus, for the next iteration ($k + 1$), the strain vector is calculated as:

$$\mathbf{X}^{k+1} = \mathbf{X}^{k} + \mathbf{F}'\left(\mathbf{X}^{k}\right)^{-1} \mathbf{F}\left(\mathbf{X}^{k}\right) \tag{28}$$

where $\mathbf{F}'$ is the Jacobian matrix of the nonlinear problem, that is:

$$\mathbf{F}' = \left(\frac{\partial \mathbf{F}}{\partial \mathbf{X}}\right) = \begin{bmatrix} f_{11} = \sum_{i=1}^{n_{lay}} E_{T,i} A_i & f_{12} = \sum_{i=1}^{n_{lay}} E_{T,i} y_i A_i \\ f_{21} = \sum_{i=1}^{n_{lay}} E_{T,i} y_i A_i & f_{22} = \sum_{i=1}^{n_{lay}} E_{T,i} y_i^2 A_i \end{bmatrix} \tag{29}$$

where $E_{t,i}$ is the tangent modulus of elasticity taken directly from the material constitutive relationship of the ith layer.

The convergence criterion adopted in this work is based on the ratio of the Euclidean norms of the unbalanced force vector, $\mathbf{F}$, and the external forces vector $\mathbf{f}_{ext}$. Thus, it is written:

$$\frac{\left\|\mathbf{F}\right\|}{\left\|\mathbf{f}_{ext}\right\|} \leq Tol \tag{30}$$

with Tol being a given tolerance, which is assumed here to be 10^{-5} (Chiorean, 2013).

The iterative process described in this section for a given external forces is illustrated in Figure 7.

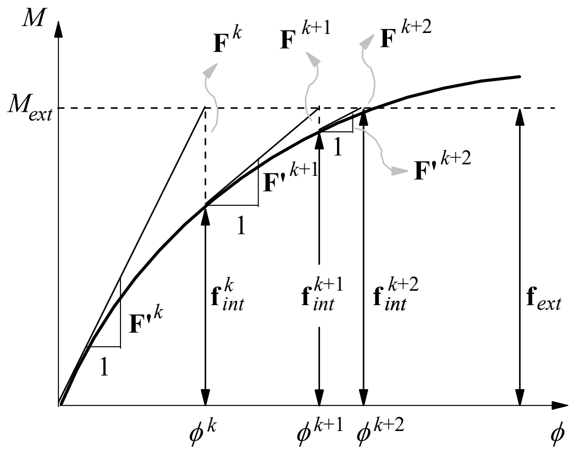

***Figure 7:** Moment-curvature relationship*

3.3 Interaction curves

The interaction curves are obtained before the structural analysis (out of incremental-iterative cycle). This strategy is adopted to reduce the execution time of the numerical simulations and it is shown in Figure 8.

Thus, the procedure described in subsection 3.2 is made for each increment of bending moment until it singularizes the Jacobian matrix (Eq. 29). Herein, the incremental strategy is given by (Zubydan, 2013):

$$M_{j+1} = M_j + \phi EI \tag{31}$$

in which the index *j* refers to the previous increment, ϕ is a constant curvature increment, *EI* is the cross-section flexural stiffness.

The initial cracking and yield curves follow the same form of construction; that is, when, for a given bending moment, the first layer reaches a strain higher than ε_{cr}, the initial cracking bending moment is reached. And when the first layer reaches the axial strain $\varepsilon_{ci}/2$ (Izzuddin and Smith, 2000), it is the initial yield bending moment.

It is necessary, however, to simplify the interaction curves. Thus, these curves are constructed by a series of ordered pairs *NM*. Once the structural analysis has been initiated, it is necessary to know the value of reduced bending moments, M_{pr}, M_{er}, and M_{cr} for a given value of axial force, *N*. Thus, any point on the interaction curve shown in Figure 9 can be obtained by linear interpolation (Lemes et al., 2017c).

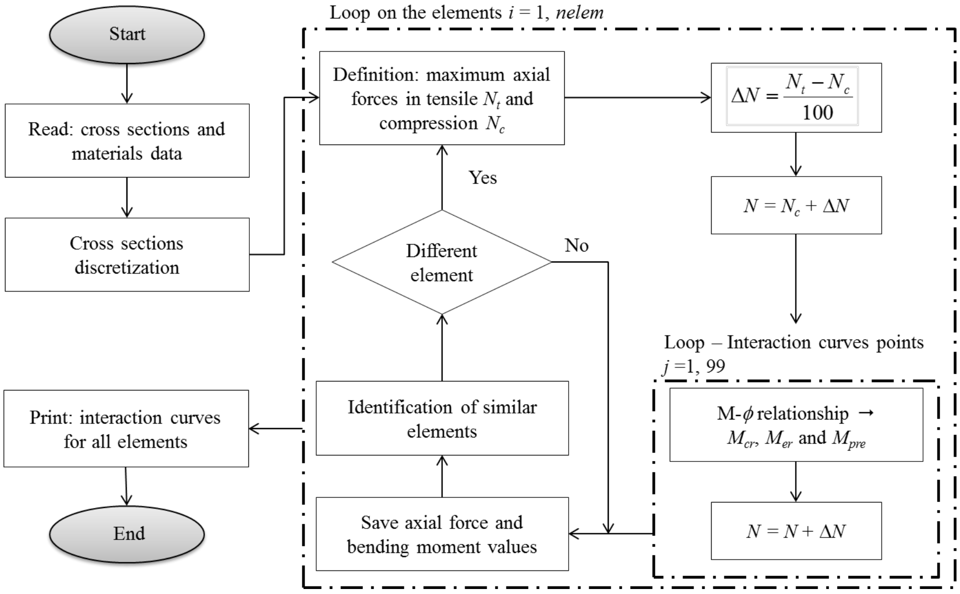

***Figure 8:** Flowchart for obtaining interaction curves*

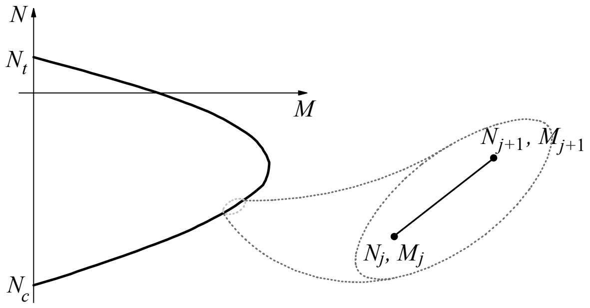

***Figure 9:** Arbitrary interaction curve points (bending moment, axial force)*

4 NUMERICAL ANALYSIS

In this section the numerical procedure described here will be tested. The proposed formulation allows for analysis of exclusively reinforced concrete (RC) structural systems. Hence, some classic problems in literature — at both the numerical and experimental levels — will be studied. The examples discussed are divided into three groups: a typical cross section analysis, Foure's column, and Cranston portal frame. A structure global mesh refinement test will be made, as the plasticity is considered in a concentrated approach. Following Lemes et al. (2017a) study, the cross section are discretized here in 16 layers.

4.1 Interaction curves in a typical RC section

Liu et al. (2012a) simulated the reinforced concrete section bearing capacity shown in Figure 10. The properties of the materials that make up the section are presented in Table 3. Two situations are analyzed here: considering (CCTS) and disregarding (DCTS) the concrete tensile strength, and the steel behavior were limited by the ultimate strain $\varepsilon_u = 0.01$. The purpose of this example is to test the local nonlinear procedure for the definition of the uncracked, elastic and bearing capacity boundaries of the RC cross-section. Thus, the major and minor axis bending are studied here.

***Table 3:** RC section: material data.*

Concrete				
f_c (kN/cm^2)	f_{cr} (kN/cm^2)	γ_c	ε_{ci}	ε_{cu}
4.0	0.269	1.5	-0.002	-0.0035
Steel				
f_y (kN/cm^2)	E_s (kN/cm^2)	γ_s	ϕ (cm)	ε_u
35.5	20500	1.15	2	0.01

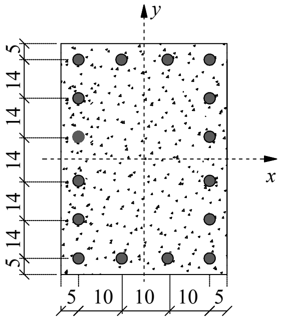

***Figure 10:** Typical RC section (dimensions in cm)*

In Figure 11, the interaction curves for the two previously described situations are shown: major and minor axis bending. One can easily see the definition of the limits described in Section 2.2 without numerical instability effects and disagreements with the expected results. Liu et al. (2012a) presents only the bearing capacity curves and the concrete tensile strength is neglected. Thus a convergence of the DCTS results with those of the said authors is observed. Other information worth mentioning is the good functioning of the stopping criterion adopted for the bearing capacity curve (singularity of the section constitutive matrix, Eq. 29). As noted by Lemes et al. (2017a), the concrete tensile strength amplifies this cross-section bearing capacity by approximately 6%.

As already expected, the initial cracking curve shows larger bending moments as the axial compression force is greater until it is coincident with the bearing capacity curve. In this latter condition, the cross section achieves its maximum strength without cracking in the section layers. In the CCTS analysis, this curve is obtained when the first layer reaches the ε_{cr} strain, and in the DCTS analysis, when the first layer presents positive axial strain.

In the initial yield curves, an angular point can be seen close to the axial compression force of 1000 kN. This point represents the change in the material influence in the definition of this curve. That is, for values greater than -1000 kN, the reinforcement is determinant and the curve is constructed when the reinforcement axial strain reaches ε_y. For N values smaller than -1000 kN, the concrete plastic strains govern the construction of this curve, being assembled when the first layer reaches ε_{cin} (Izzuddin and Smith, 2000).

Figure 12 shows the variation of the cracked moment of inertia by the axial force applied in the section for both major and minor axis. As expected, for high values of compressive axial forces the cross section reaches the critical point of the moment-curvature relationship without cracking, that is, the I_{cr} is equal to I_c (uncracked moment of inertia). Another observation is about the slight influence of the concrete tensile strength consideration. Note that in the CCTS analysis, we have higher values of I_{cr} because some layers that have low values of tensile strain can still be with an axial strain smaller than a ε_{cr}. Consequently, for axial force values close to zero or positive, a smaller cracked moment of inertia has been cracked, since the tensile stresses arising from the bending moment become more relevant.

4.2 Foure's column

Figure 13 shows the Foure's column, which was experimentally tested by Espion (1993) and then studied by several researchers (Bratina et al., 2004; Liu et al., 2012b; Iu, 2016; Lemes et al., 2017c) for validation of their numerical results. This is a fixed-free reinforced concrete column with 225 cm subjected to minor-axis bending. Such bending occurs because of an eccentricity of the vertical load applied 1.5 cm from the cross section centroid. Moreover, according to Liu et al. (2012b), this column has an initial geometric imperfection, Δ, equal to h/1000. The finite element mesh used in this example is studied varying from 1 to 6 FE. The material data are given in Table 4.

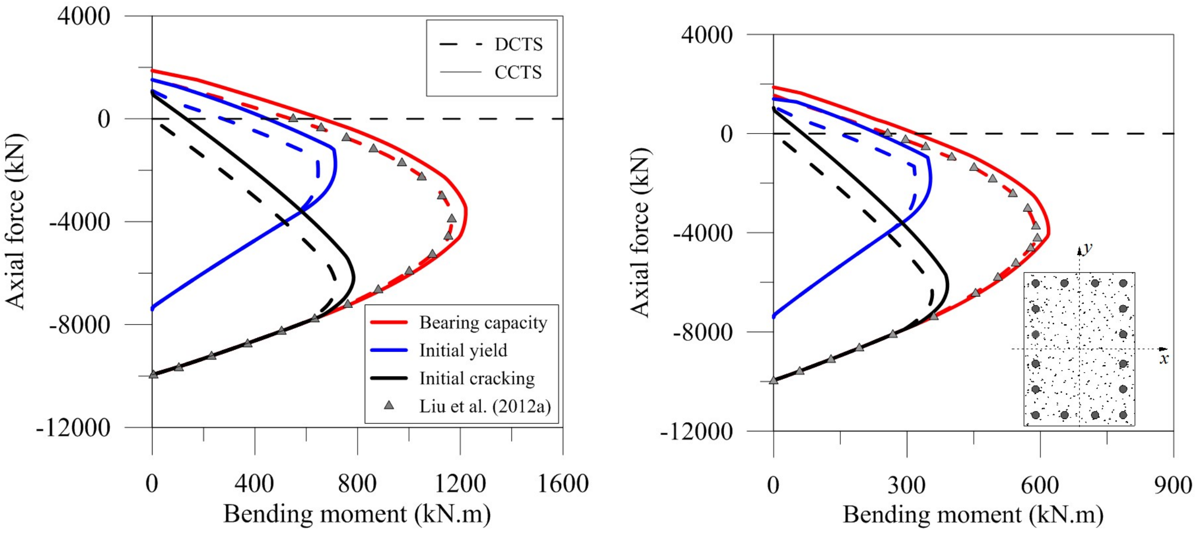

(a) Major axis bending (*x*-*x*) (b) Minor axis bending (*y*-*y*)

Figure 11: RC cross section: interaction curves

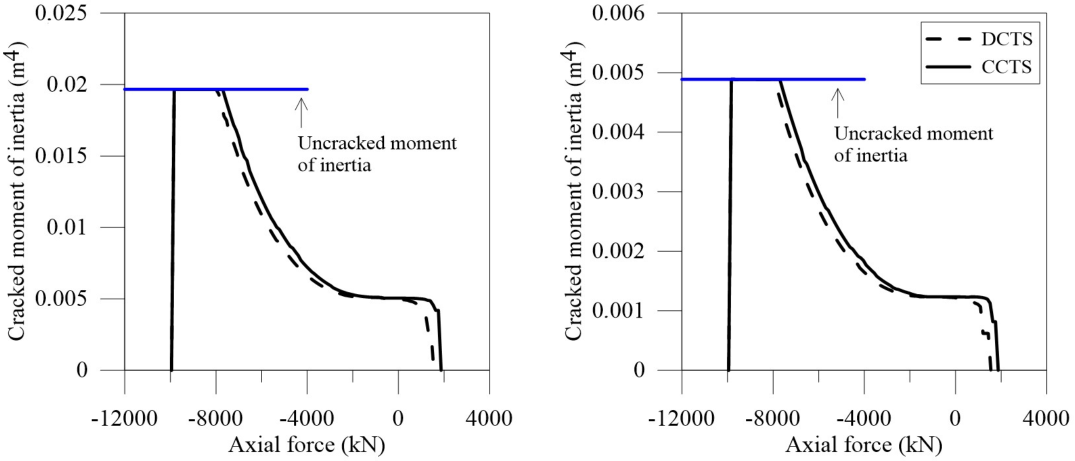

(a) Major axis bending (*x-x*) (b) Minor axis bending (*y-y*)

Figure 12: *RC cross section: cracked moment of inertia for various normal efforts*

Table 4: *Foure's column: material data.*

Concrete					Steel		
f_c (kN/cm²)	f_{cr} (kN/cm²)	E_c (kN/cm²)	ε_{ci}	ε_{cu}	f_y (kN/cm²)	E_s (kN/cm²)	ε_u
3.83	0.292	2930	-0.0023	-0.0035	46.5	20000	0.02

The study of mesh refinement is extremely important since the nonlinear effects are treated exclusively at nodal points. Thus, 6 FE meshes are tested and the results obtained using the Branson and Metz (1963) approach with each one are shown in Figure 14a. For this RC column, there is a low influence of the FE mesh in the global system response. The equilibrium paths are very close, evidencing the good convergence of the proposed formulation for low refinement indices. Another important information that can be made regarding the critical load of each tested mesh is a stabilization tendency of the critical load close to the experimental value (P_{exp} = 454 kN), visualized in Figure 14a.

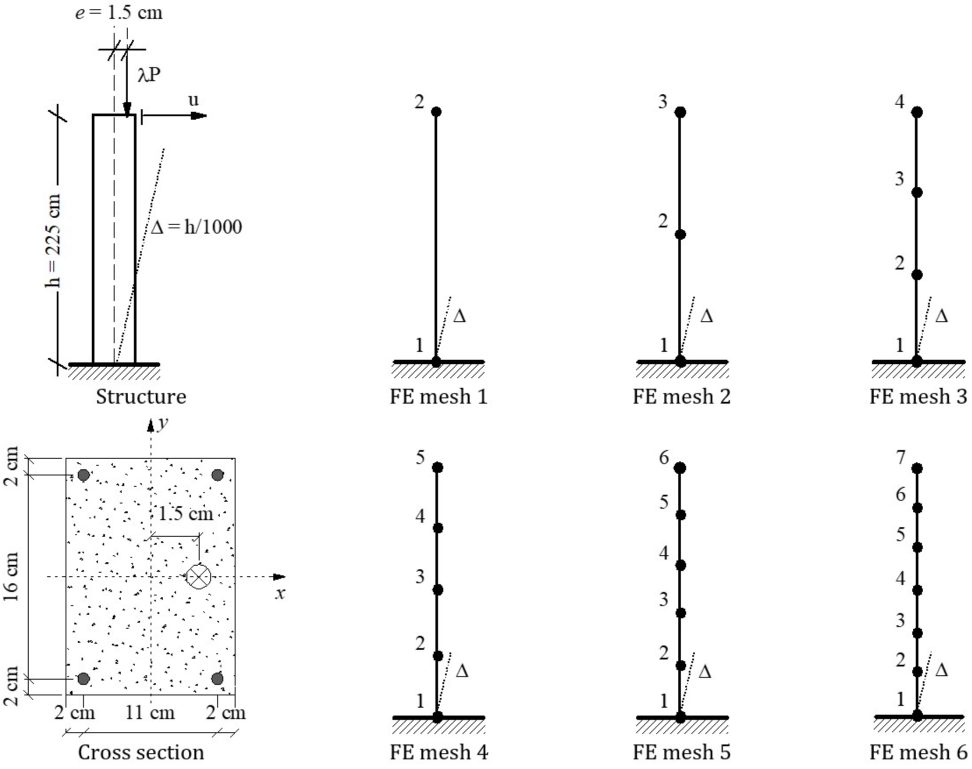

Figure 13: *Foure's column: geometry, loading, cross section and FE meshes*

The same study was carried out considering the proposal of Patel et al. (2015). Although the same previously made conclusions are adequate in these analyses, in all situations, the critical loads encountered for this condition were, on average, approximately 1.3% higher than those simulated with the BM equation, as can be seen in Figure 14b.

For the comparison with the experimental results provided by Espion (1993), it was chosen the FE mesh with 4 elements and 5 nodal points. This was defined based on the discretization adopted by Lemes et al. (2017c) and the fact that this mesh provides a critical load very close to the most refined meshes. For this same mesh, an analysis disregarding cracking effect (DCE) was performed, so it is possible to measure how important it is to consider this effect in RC structures analysis, even in elements with great influence of axial compression force.

In Figure 15 the results obtained with the numerical formulation presented in this article are plotted and compared with the test results (Espion, 1993). In general, we can see a good behavior of the equilibrium paths considering the equation of Branson and Metz (1963) - BM, and the equation of Patel et al. (2015) - P, being well adjusted to the experimental curve. However, it is worth noting that after cracking starts, $\lambda P = 383.55$ kN, the DCE analysis diverges and losing accuracy.

After the cracking starts, each of the effective moment of inertia equations presents different values, altering the system stiffness, which causes each of the equilibrium paths to reach the initial yield for different values of the incremental load, as highlighted in Figure 15.

For all numerical responses, the cracking was achieved before the material yield behavior. This observation is visible in Figure 16. The point where the greatest demand for the forces acting on the structure occurs is in the fixed support. Thus, along with the interaction curves, Lemes et al. (2017c) provided the internal force behavior at the node 1. In a brief comparison of the results obtained here, a good convergence of both can be verified with those of Lemes et al. (2017c), shown in the Figure 16. It is also worth noting that the internal forces obtained with the analysis using the BM equation are practically equal to the fibers/concentrated plasticity model of Lemes et al. (2017c).

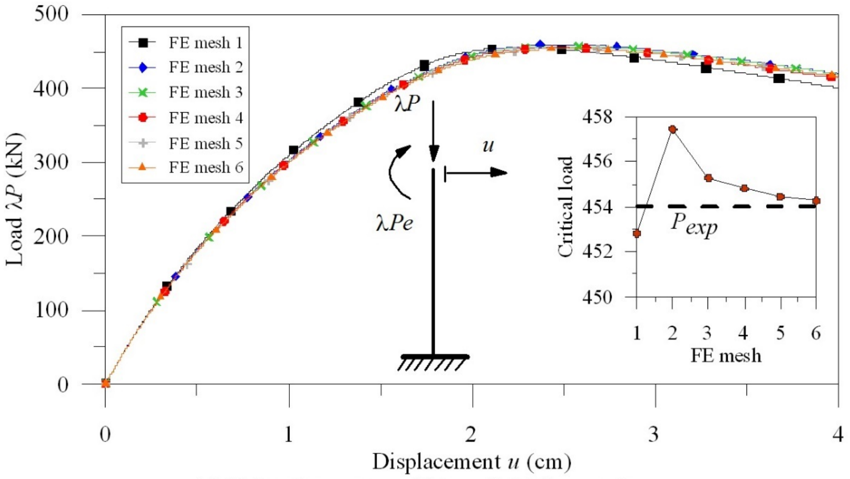

(a) Using Branson and Metz (1963) equation

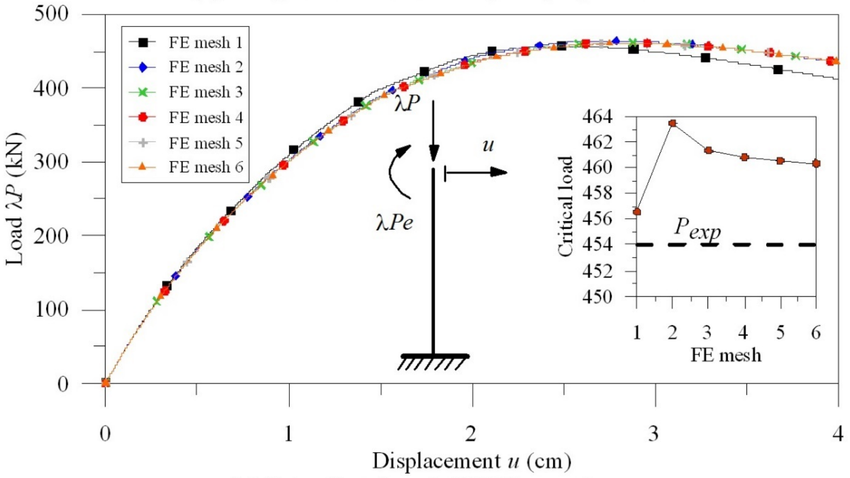

(b) Using Pattel et al. (2015) equation

Figure 14: Mesh refinement effect in equilibrium path and critical load of the structural system

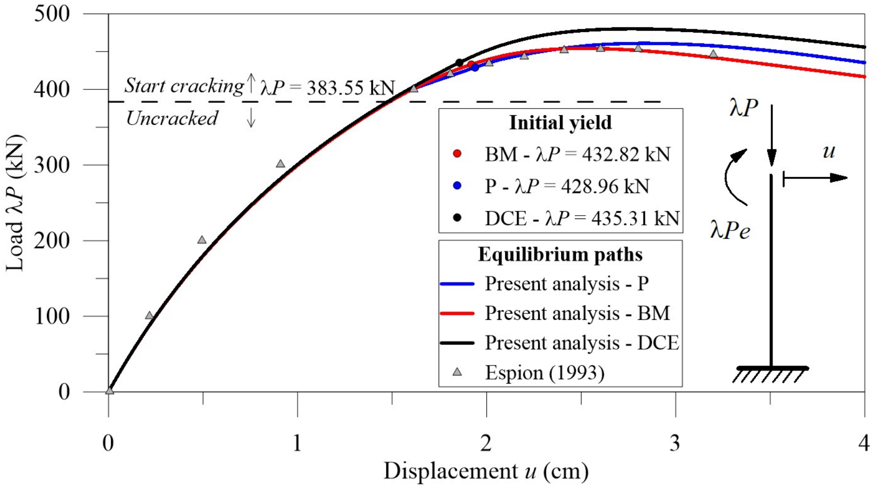

Figure 15: *Foure's column: equilibrium paths comparisons using FE mesh 4*

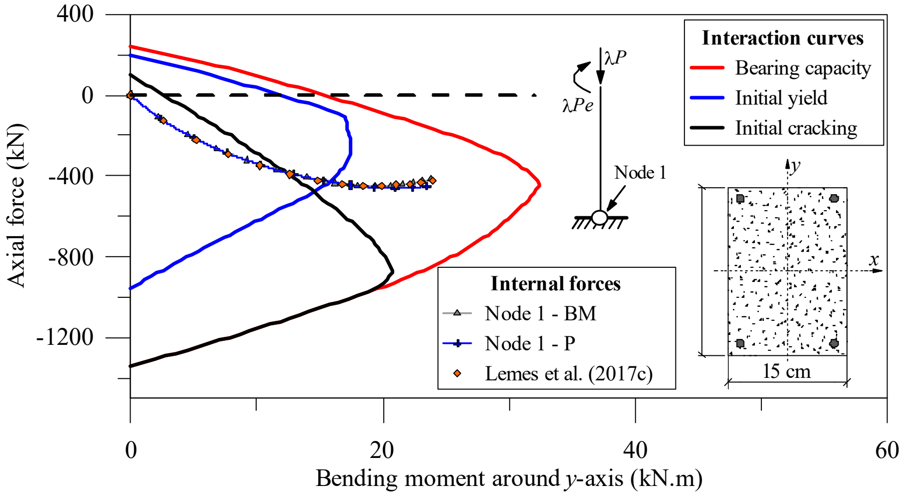

Figure 16: *Foure's column: interaction curves and internal forces in node 1 (FE mesh 4)*

Figure 16 also provides other important information. Note that the internal forces of node 1 do not reach the bearing capacity curve, that is, there are no plastic hinges in the structure. However, the combination of the forces at node 1 exceeds the initial yield curve, degrading the parameter S_p, and the initial cracking curve, changing the effective moment of inertia, I_{eq}.

Figure 17 illustrates the percentage of the pseudo-springs stiffness degradation under critical load, P_{cr}, and the displacement $u = 4$ cm. As stated previously, it is evident there are no plastic hinges in the Foure's column, since in none of the situations was a pseudo-spring with 100% degradation verified. Comparing the analysis with BM and P equations, shows that the simulation results using the P equation show higher values of degradation. This can be explained by the fact that the critical load of this analysis was found for larger displacement values, u, as can be seen in Figure 15. With greater displacements, there are higher internal bending moment values, increasing the request at the nodal points. If we compare the values found for the same displacement value, $u = 4$ cm, the analysis using P equation still has higher degradation values. Again, by looking at Figure 15, we see that in this situation the analysis using the P equation has the highest λP value, consequently increasing the internal forces in the structure.

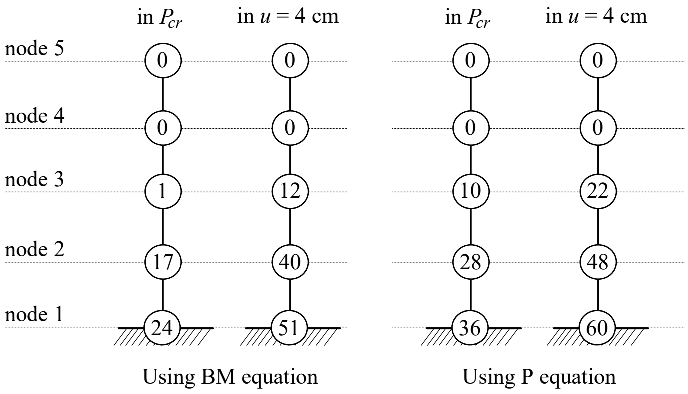

Figure 17: Percentage of the pseudo-spring rotational stiffness degradation in FE mesh 4

4.3 Two-hinge pinned portal frame

A two-hinge RC frame tested by Cranston (1965) and shown in Figure 18 is analyzed. This structure is subjected to two equally spaced incremental vertical loads inserted into the beam. Cranston (1965) provides only f_c and f_y, and the other data are taken from several researchers (Bratina et al., 2004; Valipour and Foster, 2009; Liu et al., 2012b) who simulated this frame numerically, based on Eurocode 2 (2004), and given in Table 5. All elements are under major axis bending and all reinforcement bars present diameter of 9.5 mm. The cross-sections are defined based on the nodal points of the FE mesh 1.

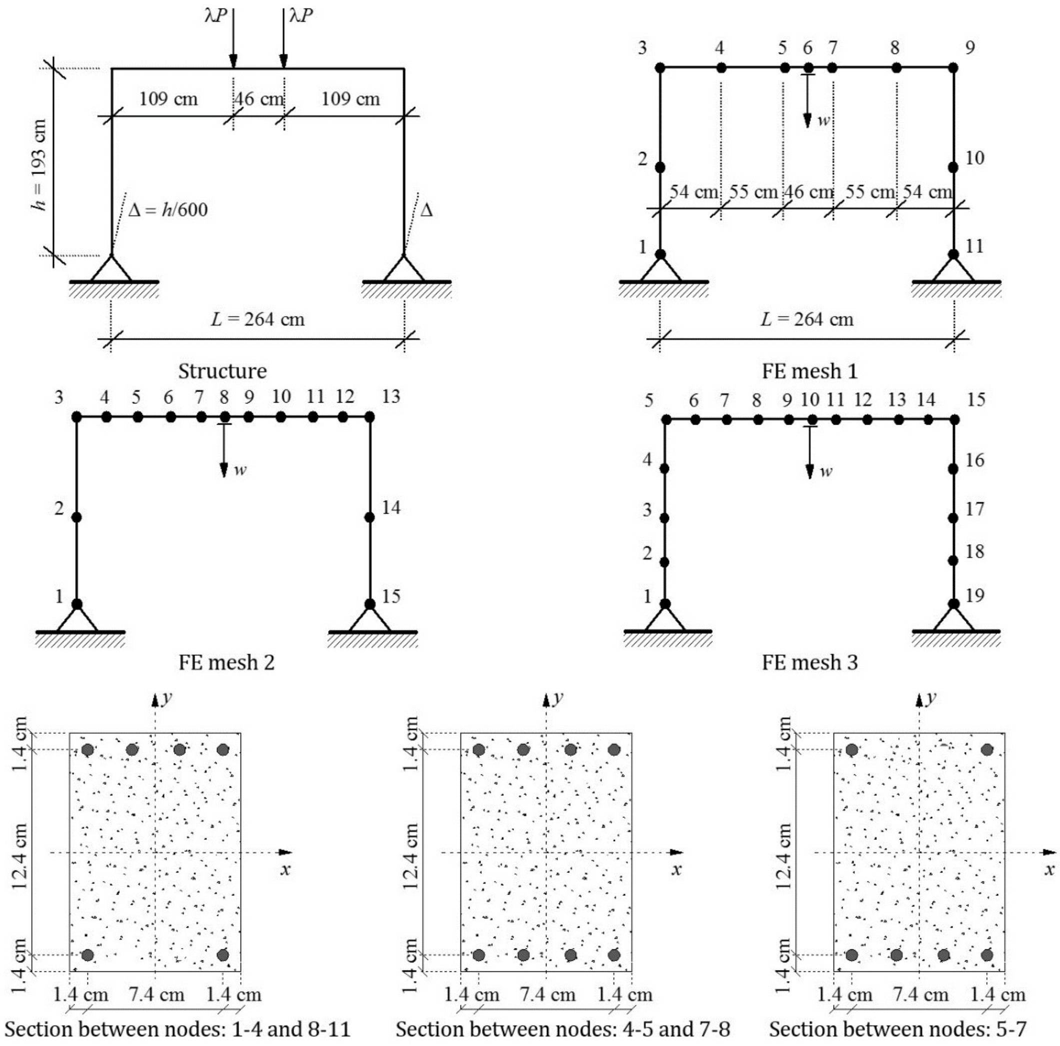

Figure 18: Cranston's portal frame: geometry, loading, cross sections and FE meshes

Table 5: Cranston's portal frame: material data.

Concrete					Steel		
f_c (kN/cm²)	f_{cr} (kN/cm²)	E_c (kN/cm²)	ε_{ci}	ε_{cu}	f_y (kN/cm²)	E_s (kN/cm²)	ε_u
3.65	0.32	2777.1	-0.0023	-0.0035	29.3	20000	0.015

Three finite element meshes are tested. Basically, FE mesh 1 is considered as the least refined mesh possible. The columns were discretized in two elements, as studied in the previous example, and the beam was divided based on the variations of cross sections in this structural element. FE meshes 2 and 3 test the influence of beam and column discretization, respectively.

As can be seen in Figure 19, the formulation presented low sensitivity to the used mesh again, using both BM and P equations. It is possible to visualize that the structure's critical load tends to a fixed value as the mesh becomes more refined. It can be noted that the critical loads were very close in both situations. In this example specifically, the values found for P_{cr} using the P equation were smaller than those found using the BM equation, unlike the previous example. Patel et al. (2015) show that the P equation presents less rigid responses than the one proposed by Branson and Metz (1963), when the beam section is already cracked. This generates a proximity in the response because, by slightly overestimating the column capacity, this equation is less conservative in relation to the beam behavior.

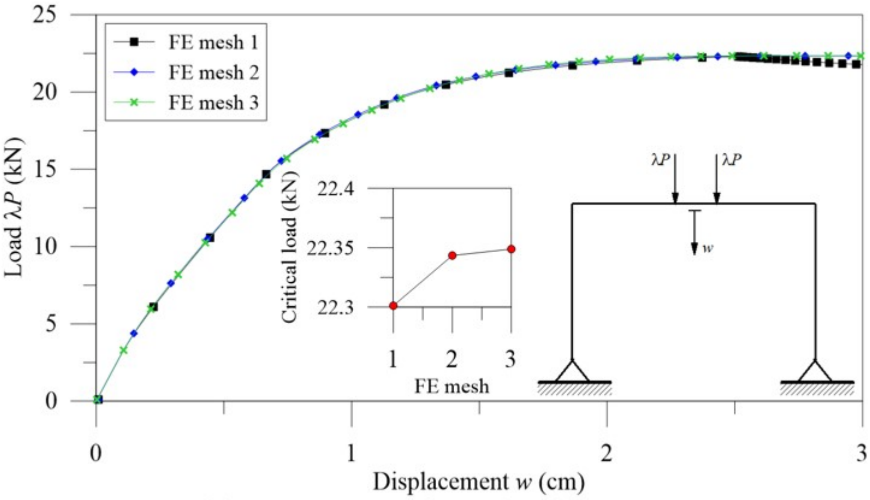

(a) Using Branson and Metz (1963) equation

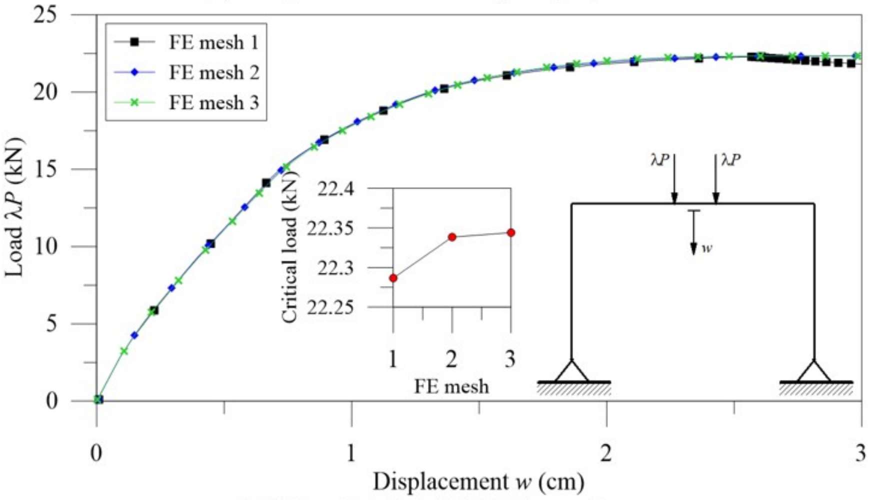

(b) Using Pattel et al. (2015) equation

Figure 19: Mesh refinement effect in equilibrium path and critical load of the structural system

FE mesh 1 presents a load limit point for displacement values somewhat smaller than the other meshes. This is due to the quick plastic hinge formation at the ends and at the center of the beam. Thus, it is possible to see in

Figure 19 a more pronounced softening in the overall behavior of this mesh. Note that the mesh refinement of the column, FE mesh 3, shows a low change in the critical load and in the equilibrium path.

It can be seen that the mesh 2 is sufficient for the structural analysis, and this mesh will be used now. Thus, the results obtained numerically are compared with those obtained by Cranston (1965). Two curves are plotted in Figure 20, load *x* displacement and bending moment at the beam left end *x* displacement. In both situations, one can observe a good proximity of the numerical and experimental curves. It is possible to highlight the good initial stiffness and the structural system critical load for both effective moment of inertia equations.

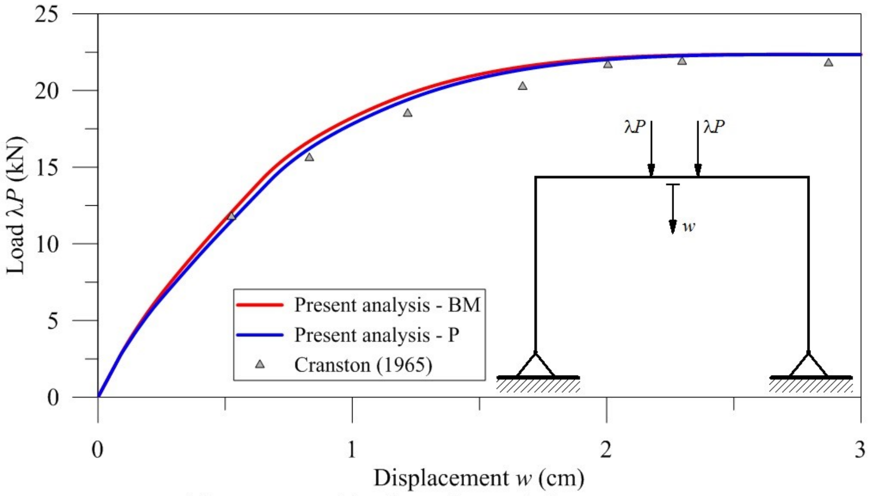

(a) Incremental load x mid span deflection curve

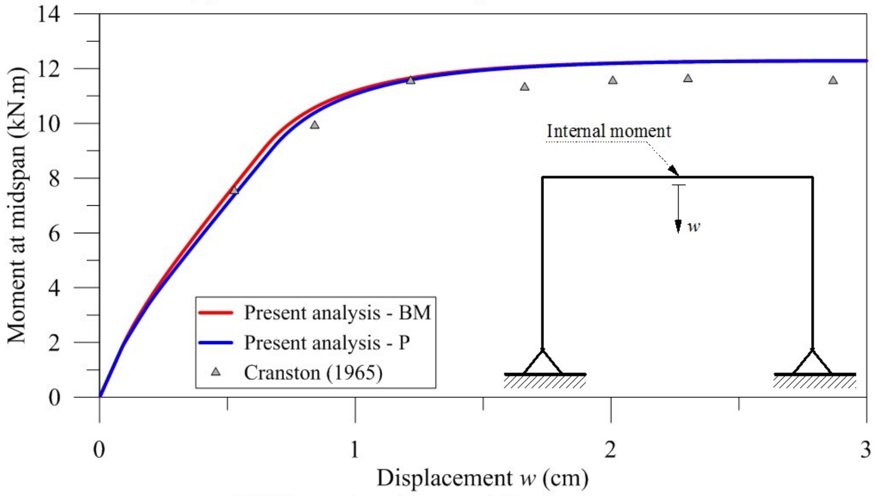

(b) Moment x mid span deflection curve

Figure 20: Cranston's portal frame: equilibrium paths

Two plastic hinges are formed along the loading history of the structural analysis. The plastic hinges are formed on nodes 3 and 13 (on the beam). Thus, due to the symmetry of the problem, it was chosen to monitor the pseudo spring stiffness degradation exclusively at node 3, as illustrated in Figure 21. In this same figure, it is possible to identify the initial and full yield moments of the cross section, indicated by dotted lines. The results obtained with both equations are coincident. This can be explained since M_{er} and M_{pr} are obtained by cross-sectional analysis, via SCM. Considering the proximity of the results obtained in Figure 21, and the internal bending moments discussed below, it can be concluded that Eq. (13) becomes practically the same.

Note that in the situation where the structure is under critical load action, the bending moment diagrams using the two effective moment of inertia equations for the cracking simulation are the same. In Figure 22, the bending moment diagram is shown and the values numerically obtained, using both (BM and P) equations are presented in Table 6.

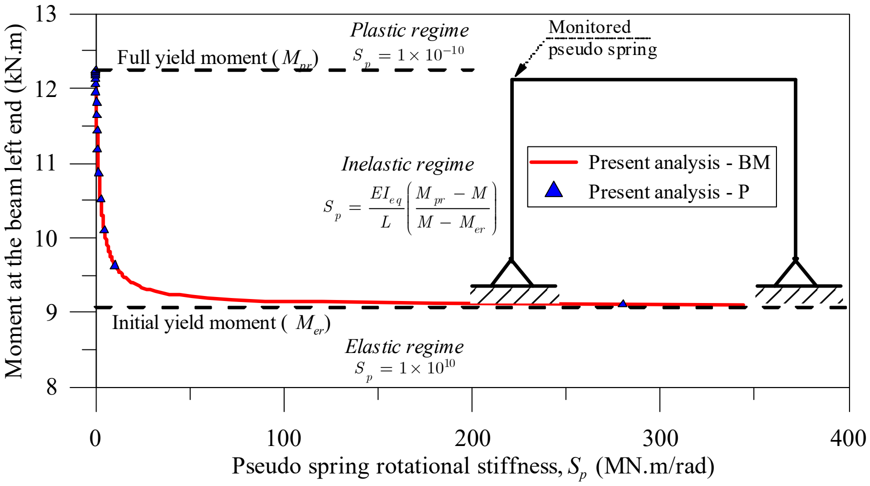

Figure 21: *Cranston's portal frame: monitoring in a plastified section*

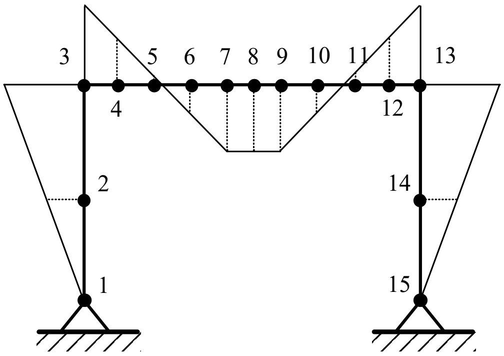

Figure 22: *Bending moment diagrams: under critical load*

Table 6: *Internal bending moments values.*

Node	Analysis	
	BM	*P*
1	0	0
2	6.2	6.2
3	12.24	12.24
4	6.17	6.17
5	0.1	0.1
6	6.08	6.08
7	12.27	12.27
8	12.28	12.28
9	12.27	12.27
10	6.08	6.08
11	0.1	0.1
12	6.17	6.17
13	12.24	12.24
14	6.2	6.2
15	0	0

5 CONCLUSIONS

This article presents a displacement-based formulation using the finite element method for physical and geometric nonlinear analysis of reinforced concrete (RC) planar structures. In this proposal, the plasticity is treated in a concentrated way using the refined plastic hinge method, where rotational pseudo springs simulate the cross section flexural stiffness degradation. Cracking is also approached through the effective moment of inertia of the section, considered through two approaches: Branson and Metz (1963) and Patel et al. (2015). Some general conclusions can be made:

- isolated beams were not analyzed, since the Cranston portal frame has its nonlinear material behavior with greater beam influence, both in the plasticity and cracking context;
- low refinement indices were sufficient for a satisfactory global response in the two examples tested;
- the use of the effective moment of inertia equation of RC elements improves the analyses accuracy, since the cracking is an inherent problem of concrete elements under tensile stress;
- more refined meshes tend to convergent solutions without presenting numerical instabilities and critical load oscillations of the simulated structural systems; and
- the proposal of union of the classical RPHM with the effective moment of inertia equation provided satisfactory results in the context of nonlinear analysis of planar RC structures.

More specifically, in the comparison of the effective moment of inertia equations, we highlight:

- both equations were developed for beams. An adjustment in the cracked moment of inertia was necessary to allow them to be used in columns/frames analysis;
- as observed by Patel et al. (2015), the P equation provides less rigid responses to post-cracking beams when compared to the BM equation. This observation can be seen by analyzing the two examples tested, in the Foure's column there was a higher critical load when the P equation was used. In the Cranston portal frame, as the beam presents higher cracking rates, it is possible to see that the situation is reversed, and the results are obtained through the equation P are more conservative than the BM equation.

As future work, we intend to develop an equation capable of describing the variation of the cross section effective moment of inertia in a cracking regime for elements submitted to combined efforts (N x M) and apply it to the global formulation presented here. Although the results obtained have already presented considerable precision, high order terms can be included in the geometric nonlinear formulation to improve the accuracy in the analyses of large RC structures.

Acknowledgments

The authors would like to thank CAPES and CNPq (Federal Research Agencies), Fapemig (Minas Gerais State Research Agency), and UFOP for their support during the development of this work. Special thanks go to prof. Harriet Reis for the editorial review of this text.

References

ACI-318, (2008). Building code requirements for reinforced concrete. American Concrete Institute.

Al-ZaidD, R.Z., Al-Shaikh, A.H., Abu-Hussein, M.M., (1991). Effect of loading type on the effective moment of inertia of reinforced concrete beams. ACI Structural Journal 88(2): 184-190.

Bischoff, P.H., (2005). Reevaluation of deflection prediction for concrete beams reinforced with steel and fiber reinforced polymer bars. Journal of Structural Engineering 131(5): 752-762.

Branson, D.E. & Metz G.A., (1963). Instantaneous and time-dependent deflections of simple and continuous reinforced concrete beams. Auburn: Dept. of Civil Engineering and Auburn Research Foundation, Auburn University.

Bratina, S., Saje, M. & Planinc, I., (2004). On materially and geometrically non-linear analysis of reinforced concrete planar frames. International Journal of Solids and Structures 41(24): 7181-7207.

Caldas, R.B., (2004). Numerical analysis of steel-concrete composite columns, M. Sc. Dissertation (in Portuguese), Federal University of Ouro Preto, Brazil.

Carvalho, R.C. & Figueiredo Filho, J.R., (2014). Calculation and detailing of usual reinforced concrete structures according to NBR 6118: 2014. EdUFSCar, São Carlos (in Portuguese).

Chan, S.L., (1988). Geometric and material non-linear analysis of beam-columns and frames using the minimum residual displacement method. International Journal of Numerical Methods in Engineering 26(12): 2657–2669.

Chan, S.L. & Chui, P., (2000). Non-linear static a cyclic analysis of steel frames with semi-rigid connections. Oxford, Elsevier.

Chen, W. & Kim, S., (1997). LRFD Steel Design using Advanced Analysis. Boca Raton, Flórida, EUA: CRC Press.

Chiorean, C.G., (2013). A computer method for nonlinear inelastic analysis of 3D composite steel-concrete frame structures. Engineering Structures 57: 125-152.

Cranston, W.B. (1965). Tests on reinforced concrete frames, 1: Pinned portal frames. Technical Report TRA/392, Cement and Concrete Association, London, England.

Espion, B., (1993). Benchmark Examples for Creep and Shrinkage Analysis Computer Programs, Creep and Shrinkage of Concrete. TC 114 RILEM. E&FN Spon.

Eurocode 2, (2004). Design of concrete structures-Part 1-1: General rules and rules for buildings. European Committee for Standardization.

Fong, M. & Chan, S. L., (2012). Advanced analysis of steel-concrete composite beam-columns by refined plastic-hinge method. International Journal of Structural Stability and Dynamics 12(6), 1250046.

Gilbert, R.I., (1999). Deflection calculation for reinforced concrete structures- why we sometimes get it wrong. ACI Structural Journal 96(6): 1027-1033.

Iu, C. K., (2016). Nonlinear analysis of the RC structure by higher-order element with the refined plastic hinge. Computers and Concrete 17(5): 579-596.

Izzuddin, B.A. & Smith, D.L., (2000). Efficient nonlinear analysis of elasto-plastic 3D R/C frames using adaptive techniques. Computers and Structures 78(4): 549–573.

Kostic, S.M. &, Filippou, F.C., (2012). Section discretization of fiber beam–column elements for cyclic inelastic response. Journal of Structural Engineering 138(5): 592–601.

Lemes, Í.J.M., (2015). Advanced analysis via RPHM of steel-concrete composite structures, M. Sc. Dissertation (in Portuguese), Federal University of Ouro Preto, Brazil.

Lemes, Í.J.M., Silva, A.R.D, Silveira, R.A.M., Rocha, P.A.S., (2016). Comparative numerical study of methodologies for the flexural stiffness degradation in the context of the Refined Plastic Hinge Method. XXXVI Ibero-Latin American Congress on Computational Methods in Engineering (in Portuguese).

Lemes Í.J.M., Silva, A.R.D, Silveira R.A.M & Rocha, P.A.S., (2017a). Determination of the bearing capacity of composite structural elements through the Refined Plastic Hinge Method. Revista Internacional de Métodos Numéricos para Cálculo y Diseño en Ingeniería 33,(1-2): 24-34 (in Portuguese).

Lemes Í.J.M., Silva, A.R.D., Silveira, R.A.M & Rocha P.A.S., (2017b). Numerical analysis of nonlinear behavior of steel-concrete composite structures. Revista IBRACON de Estruturas e Materiais 10(1): 53-83.

Lemes Í.J.M., Silveira, R.A.M, Silva, A.R.D. & Rocha P.A.S., (2017c). Nonlinear analysis of two-dimensional steel, reinforced concrete and composite steel-concrete structures via coupling SCM/RPHM. Engineering Structures 147: 12-26.

NBR-6118, (2014). Design of concrete structures - procedure. Brazilian Association of Technical Standards (ABNT), Rio de Janeiro, Brazil, (in Portuguese).

Liu, S.W., Liu Y.P & Chan, S.L., (2012a) Advanced analysis of hybrid steel and concrete frames Part 1: Cross-section analysis technique and second-order analysis. Journal of Constructional Steel Research 70: 326-336.

Liu, S.W., Liu Y.P & Chan, S.L., (2012b) Advanced analysis of hybrid steel and concrete frames Part 2: Refined plastic hinge and advanced analysis. Journal of Constructional Steel Research 70: 337-349.

Ngo-Huu, C. & Kim, S.E., (2012). Practical nonlinear analysis of steel-concrete composite frames using fiber-hinge method. Journal of Constructional Steel Research 74: 90-97.

Parente Jr, E., Nogueira, G. V., Meireles Neto, M. & Moreira, L. S., (2014). Material and geometric nonlinear analysis of reinforced concrete frames. Revista IBRACON de Estruturas e Materiais 7(5): 879-904.

Patel K.A., Bhardwaj, A., Chaudhary, S. & Nagpal A.K., (2015). Explicit expression for effective moment of inertia of RC beams. Latin American Journal of Solids and Structures 12(3): 542-560.

Scott, M.H. & Fenves, G.L., (2006). Plastic-hinge integration methods for force-based beam-column elements. Journal of Structural Engineering 132(2):244–252.

Sousa Jr. J.B.M., & Caldas R.B., (2005). Numerical analysis of composite steel-concrete columns of arbitrary cross section. Journal of Structural Engineering 131(11): 1721-1730.

Sousa Jr., J.B.M., & Muniz, C.F.D.G., (2007). Analytical integration of cross section properties for numerical analysis of reinforced concrete, steel and composite frames. Engineering Structures 29(4): 618–625.

Spacone, E., Filippou, F.C. & Taucer, F.F., (1996). Fibre beam-column model for non-linear analysis of R/C frames: Part I. Formulation. Earthquake Engineering and Structural Dynamics 25(7): 711-725.

Stramandinoli, R.S.B., (2007). Finite element models for nonlinear physical and geometric analysis of beams and plane frames concrete structures. M. Sc. Dissertation (in Portuguese). Federal University of Santa Catarina.

Tikka, T.K. & Mirza, S.A., (2005). Nonlinear El equation for slender reinforced concrete columns. ACI Structural Journal 102(6): 839–848.

Valipour, H. R., & Foster, S. J. (2009). Nonlocal damage formulation for a flexibility-based frame element. Journal of Structural Engineering, 135(10), 1213-1221.

Vecchio, F.J. & Collins, M.P., (1986). The modified compression field theory for reinforced concrete elements subjected to shear. ACI Journal 83: 219–231.

Yang, Y.B. & Kuo, S.B., (1994). Theory & Analysis of Nonlinear Framed Structures. Prentice Hall.

Zubydan, A.H., (2013). Inelastic Large Deflection Analysis of Space Steel Frames Including H-shaped Cross-Sectional Members. Engineering Structures 48: 155-165.